arXiv:1703.04673v1 [cond-mat.mtrl-sci] 14 Mar 2017

Dirac dispersion and non-trivial Berry's phase in three-dimensional semimetal $RhSb_3$

Kefeng Wang,[1] F. Boschini,[2,3] B. J. Ramshaw,[4] D. Graf,[5] Limin Wang,[1] M. Michiardi,[2,3] A. Zonno,[2,3] E. Rotenberg,[6] A. Bostwick,[6] A. Damascelli,[2,3,7] and J. Paglione[1,7]

[1] *Center for Nanophysics and Advanced Materials, Department of Physics, University of Maryland, College Park, MD 20742, USA*
[2] *Department of Physics and Astronomy, University of British Columbia, Vancouver, BC V6T 1Z1, Canada*
[3] *Quantum Matter Institute, University of British Columbia, Vancouver, BC V6T 1Z4, Canada*
[4] *Pulsed Field Facility, National High Magnetic Field Laboratory, Los Alamos National Laboratory, Los Alamos, NM 87545*
[5] *National High Magnetic Field Laboratory, Florida State University, Tallahassee, FL 32306-4005, USA*
[6] *Advanced Light Source, Lawrence Berkeley National Laboratory, Berkeley, CA 94720, USA*
[7] *Canadian Institute for Advanced Research, Toronto, Canada M5G 1Z8*

(Dated: March 16, 2017)

We report observations of magnetoresistance, quantum oscillations and angle-resolved photoemission in $RhSb_3$, a unfilled skutterudite semimetal with low carrier density. The calculated electronic band structure of $RhSb_3$ entails a Z_2 quantum number $\nu_0 = 0, \nu_1 = \nu_2 = \nu_3 = 1$ in analogy to strong topological insulators, and inverted linear valence/conduction bands that touch at discrete points close to the Fermi level, in agreement with angle-resolved photoemission results. Transport experiments reveal an unsaturated linear magnetoresistance that approaches a factor of 200 at 60 T magnetic fields, and quantum oscillations observable up to 150 K that are consistent with a large Fermi velocity ($\sim 1.3 \times 10^6$ ms^{-1}), high carrier mobility ($\sim 14\ m^2$/Vs), and small three dimensional hole pockets with nontrivial Berry phase. A very small, sample-dependent effective mass that falls as low as 0.015(7) bare masses scales with Fermi velocity, suggesting $RhSb_3$ is a new class of zero-gap three-dimensional Dirac semimetal.

PACS numbers: 72.20.My,72.80.-r,75.47.Np

INTRODUCTION

Following the discovery of topological insulators [1, 2], new classes of topological materials such as Dirac semimetals [3], Weyl semimetals [4, 5], nodal line and nodal chain semimetals [6, 7], have received considerable interest. In Dirac systems, linearly dispersing valence and conduction bands touch at discrete points of fourfold degeneracy in the Brillouin zone (BZ), giving Dirac nodes protected against gap formation by crystal symmetry. Cd_3As_2 and Na_3Bi were the first theoretically predicted Dirac semimetal candidates,[8, 9] later confirmed by experiments [10–13]. By breaking either inversion or time reversal symmetry, a Dirac semimetal can be tuned to a Weyl state where the nondegenerate linear touchings of the bulk bands come in pairs [4, 5], confirmed by recent experiments on materials such as the TaAs family (Type-I), WTe_2 and $MoTe_2$ (Type-II) [14–17]. The topologically nontrivial band structure in such materials could host unusual electronic states and exotic physical properties, including the chiral anomaly and the associated negative magnetoresistance (MR), non-local transport and the quantum anomalous Hall effect [18–25]. More interesting, most topological semimetals exhibit very high mobilities and extremely large MR [18, 19, 21, 23–26]: carrier mobilities in Cd_3As_2, TaAs, and WTe_2 approach $1 \sim 100$ m^2/Vs, and MR records of up to ~ 5000 are observed in only in 9 T fields. Extreme MR was also observed in LaSb, $NbSb_2$, $TaAs_2$ and $NbAs_2$, which also show signs of topological properties [27–30]. The mechanism of this extremely large MR is still not clear, but is believed to arise from the lifting of the protecting high mobility or high mobility fluctuations due to the disorder effect of the Dirac quasiparticles.[18, 19]

Although there has been extensive studies of many topological semimetals, the materials belonging to these two categories are still rare, making it imperative to explore more candidates and their physical properties. $CoSb_3$, with the original unfilled skutterudite structure, is a well known thermoelectric small gap semiconductor [31] found to have quasilinear valence and conduction bands many years ago [32]. Although it is topologically trivial, it was recently revealed that the displacement of Sb sublattices could induce a band inversion and a transition from a trivial state to topological insulator when spin-orbit coupling opens a gap through a critical point in which massless (Dirac or Weyl) bands appear[33, 34]. Similar behavior was also proposed in the theoretical compound $IrBi_3$, where band inversion between Ir-d and Bi-p orbtitals was predicted to occur [35].

In this work, we report several experimental properties that suggest the unfilled skutterudite material $RhSb_3$ represents a new family of non-trivial three-dimensional topological Dirac semimetals. Together with observations of very large MR and carrier mobility values, quantum oscillations studies of the effective mass and nontrivial Berry's phase as well as angle-resolved photoemission spectroscopy (ARPES) experiments are consistent

with first-principle calculations of the electronic structure that indicate an inverted band Dirac dispersion.

EXPERIMENTAL DETAILS

Single crystals of $RhSb_3$ were synthesized by a high-temperature self-flux method. X-ray diffraction data were taken at room temperature with Cu K_α (λ = 0.15418 nm) radiation in a powder diffractometer. Electrical transport measurements up to 14 T were conducted on polished samples in a commercial cryostat applying the conventional four-wire contact method. High field MR and Shubnikov-de Haas (SdH) oscillation were measured at the National High Magnetic Field Laboratory (NMMFL) Tallahassee DC Field Facility up to 35 T, using a one-axis rotator in a He-3 cryostat with temperature range 0.35 K $\sim$ 70 K, and also at the NHMFL Los Alamos pulsed field facility up to 60 T field. All measurements were performed with electrical current flowing along the [100] direction. Magnetic field direction was always kept perpendicular to current, but rotated from perpendicular to (100) face ($\theta = 0^o$) to direction along (100) face ($\theta = 90^o$). ARPES measurements were performed at beamline 7.0.2.1 of the Advanced Light Source (ALS) at Lawrence Berkeley National Laboratory. The sample was cleaved and kept at 80 K at a base pressure of 5×10^{-11} Torr. Photoemitted electrons were detected with a Scienta R4000 analyser, for photon energy ranging from 90 to 170 eV. The energy and the angular resolution were better than 50 meV and 0.2^o, respectively. First principles electronic structure calculations were performed within the full-potential linearized augmented plane wave (LAPW) method [36] implemented in WIEN2k package.[37] The general gradient approximation (GGA) of Perdew *et al.*,[38] was used for exchange-correlation potential. The LAPW sphere radius were set to 2.5 Bohr for all atoms. The converged basis corresponding to $R_{min}k_{max} = 7$ with additional local orbital were used, where R_{min} is the minimum LAPW sphere radius and k_{max} is the plane wave cutoff. Lattice parameters were obtained from refinement of the x-ray diffraction pattern obtained from powdered single crystals.

RESULTS AND DISCUSSION

$RhSb_3$ crystallizes in the skutterudite structure (space group $Im\bar{3}$) with cubic Bravais lattice. Earlier studies have shown that the family of TSb_3 (T=Co and Ir) have quasi-linear valence/conduction bands [32–34]. Although these linear bands are topologically trivial and gapped by spin-orbit coupling (SOC), it has recently been shown that the displacement of the Sb sublattice could induce a transition from trivial insulator to topological point Fermi surface (FS) system through a critical point with massless Dirac band [33]. $RhSb_3$, instead, has an inverted band structure and is a point FS, zero-gap topological semimetal. SOC lifts the three-fold degenerate band structure at $k = 0$ to a two-fold degenerate structure (left panel of Fig. 1(b)). In the valence band, the part far away from the Γ point is mainly contributed from p-orbital of Sb atoms. However, the weight of Rh-4d orbital (indicated by the radii of circles in the band line of Fig. 1(b)) increases when approaching the Fermi level and then becomes dominant. This clearly indicates a band inversion between Rh$-d$ and Sb-p orbitals, also predicted for the theoretical compound $IrBi_3$ [35]. Moreover, the conduction and valence bands touch at points slightly away from the Γ point along the Γ-N line. These bands are fairly linear close to the Fermi level.

To evaluate and confirm the non-trivial topology of these bands, we employ the method proposed by Fu and Kane [39] to calculate the Z_2 invariant ν_0. Considering the eight time-reversal invariant momenta (TRIM) in the first BZ (as listed in the first column of Fig. 1(c)), Z_2 invariant for the N valence bands $\nu_0(N)$ is expressed as $(-1)^{\nu_0(N)} = \prod_{i=1}^{8} \delta_i$ where $\delta_i = \prod_{m=1}^{N} \xi_m(\Gamma_i)$ is the product of parity eigenvalue ($\xi_m(\Gamma_i) = \pm 1$) of the mth band at ith TRIM Γ_i. We considered 36 valence bands from the Fermi level ($N = 36$) since they are well isolated at -6 eV from others. The resulted δ_is are listed in Fig. 1(c) and it gives Z_2 quantum number $\nu_0 = 1, \nu_1 = \nu_2 = \nu_3 = 0$, indicating its analogy to strong topological insulator. In the energy region above $\sim$ 15 meV, a Lifshitz transition as a function of doping occurs and the FS changes from isolated small elliptical pockets (the left panel of Fig. 1(d)) to a larger merged anisotropic pocket centered at Γ point (the middle panel of Fig. 1(d)). At higher doping, the FS becomes more isotropic (right panel in Fig. 1(d)).

Photon-energy dependent ARPES measurements confirm the presence of a linearly-dispersive three-dimensional hole pocket around Γ. The sample was cleaved exposing the (100) surface. Assuming a 10 eV inner potential, at 140 eV photon energy the momentum probed along the c axis corresponds to $k_z \sim 4.5 \times 2\pi/c$ ($\pi/c = \Gamma - H$). One should note that, as a consequence of the body-centered cubic structure, the Γ points from adjacent surface-projected BZs are characterized by a π/c offset in k_z. For this reason, hole-like FS pockets can be observed in Fig. 2(a) only around the Γ points of the 2nd BZ. Furthermore, due to matrix element effects, using linear horizontal polarization (p) the 2nd BZ hole pockets can be detected only along the $k_x = 0\mathring{A}^{-1}$ line while, with linear vertical polarization (s), those same pockets are observed exclusively along the $k_y = 0\mathring{A}^{-1}$ line (Suppl. Mat.). The ARPES band mapping along k_x, k_y and k_z directions is presented in Fig. 2(b). As a consequence of matrix elements effects and to maximize the photoemission intensity from the hole pocket, these three cuts have been acquired in different regions

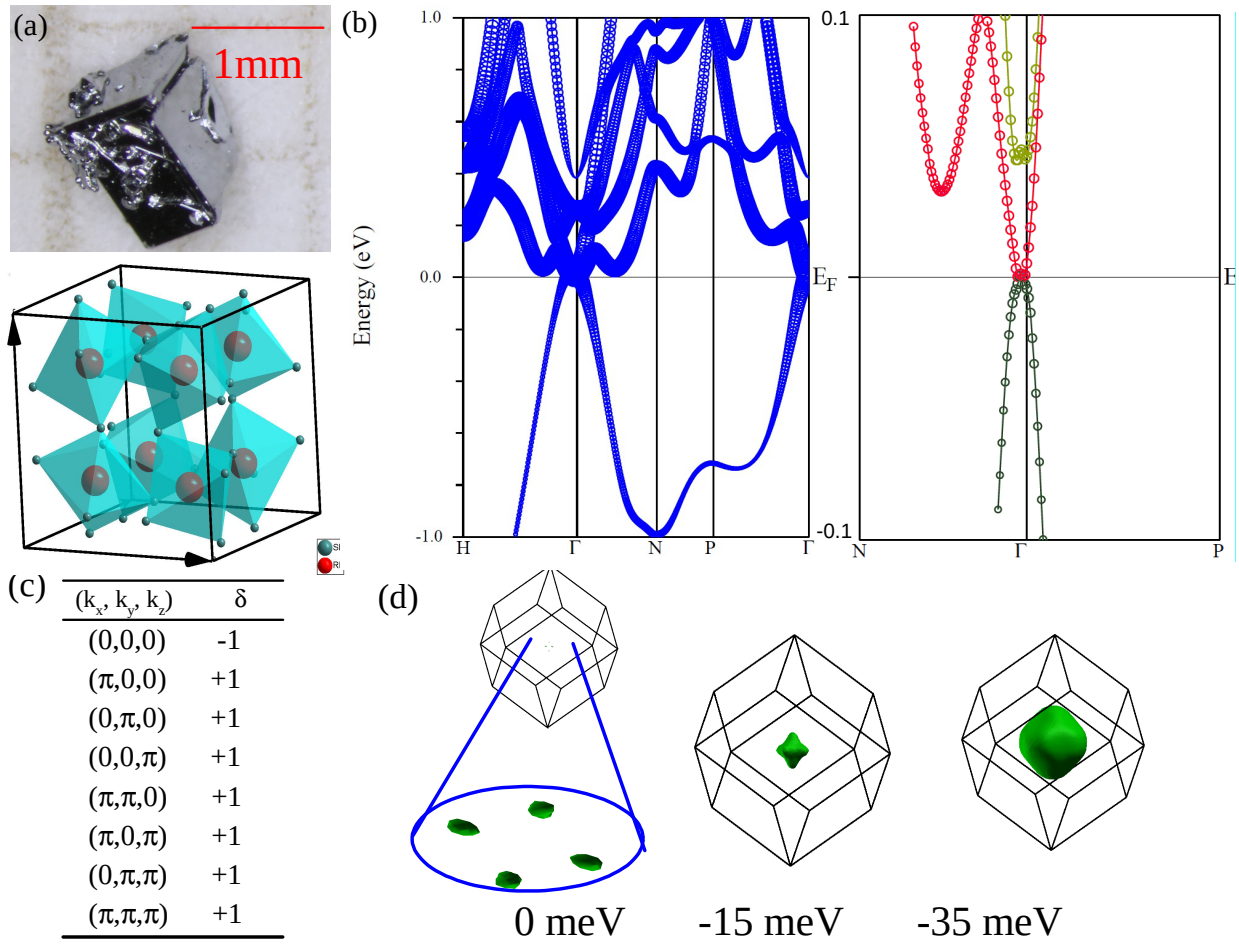

(k_x, k_y, k_z)	δ
(0,0,0)	-1
(π,0,0)	+1
(0,π,0)	+1
(0,0,π)	+1
(π,π,0)	+1
(π,0,π)	+1
(0,π,π)	+1
(π,π,π)	+1

FIG. 1. Crystal and calculated electronic structure in $RhSb_3$. (a) The image of a typical single crystal and schematic structure of $RhSb_3$. (b) The band structure of $RhSb_3$ from first-principle calculation with spin-orbit coupling. The radii of the circles in the band lines are proportional to the weight of Rh-4*d* orbital. (c) Parity of the TRIM of the Brillouin zone. Calculated based on the DFT with SOC. (d) The FS represented in the first Brillouin zone by shifting rigidly the chemical potential down at three different values. In zero-energy shift (left column), the very small pockets are shown in the lower part by enlarged 50 times.

of momentum space using different photon energies and incident polarizations. The left-hand side and central panels of Fig. 2(b) present the band mapping along the k_x and k_y directions [yellow and white dashed lines in (a), respectively]. By fitting the momentum distribution curves in the left panel, we estimate a Fermi velocity of $0.6(\pm 0.2) \times 10^6$ m/s ($4 \pm 1.2 eV\mathring{A}$). Finally, in order to verify the three-dimensional nature of the detected pocket, we performed a photon-energy scan. The right panel in Fig. 2(b) displays how the photoemission intensity at $(k_x, k_y) = (-0.57\mathring{A}^{-1}, 0\mathring{A}^{-1})$, slightly off the Γ point [orange circle in (a)], changes as the function of the probed k_z, and qualitatively defines a cone-like dispersion. Thus this hole pocket exhibits an almost isotropic three-dimensional dispersion, in good agreement with band structure calculations for this compound and at variance with what is instead observed for Cd_2As_3, where the Fermi velocity is markedly anisotropic.[12]

Magnetic fields applied along the a-axis (perpendicular to (100) face) significantly enhance the resistivity of $RhSb_3$. The MR ($MR = (\rho_{xx}(B) - \rho_{xx}(0))/\rho_{xx}(0)$) does not show any sign of saturation up to a 64 T pulsed field (Fig. 3(a)) but exhibits quantum oscillations above about 10 T (also observed in Hall resistivity, Fig. 3(b)), and continues to increase above the quantum limit of $\sim$ 35 T. The MR ratio is close to the reported value ($10^3 \sim 10^6$) of that observed in both the Dirac material Cd_3As_2 and TaAs Weyl family. [18, 19, 21, 23–26] Beside the large MR, the magnetic field also induces a change in the temperature dependence of the resistivity. $RhSb_3$ exhibits semimetallic behavior in the absence of magnetic field, where the resistivity decreases with decreasing temperature but then approaches a saturated value below 20 K, as shown in Fig. 3(c). In fields above 1 T, the resistivity changes from positive temperature dependence to negative below a distinct crossover temperature

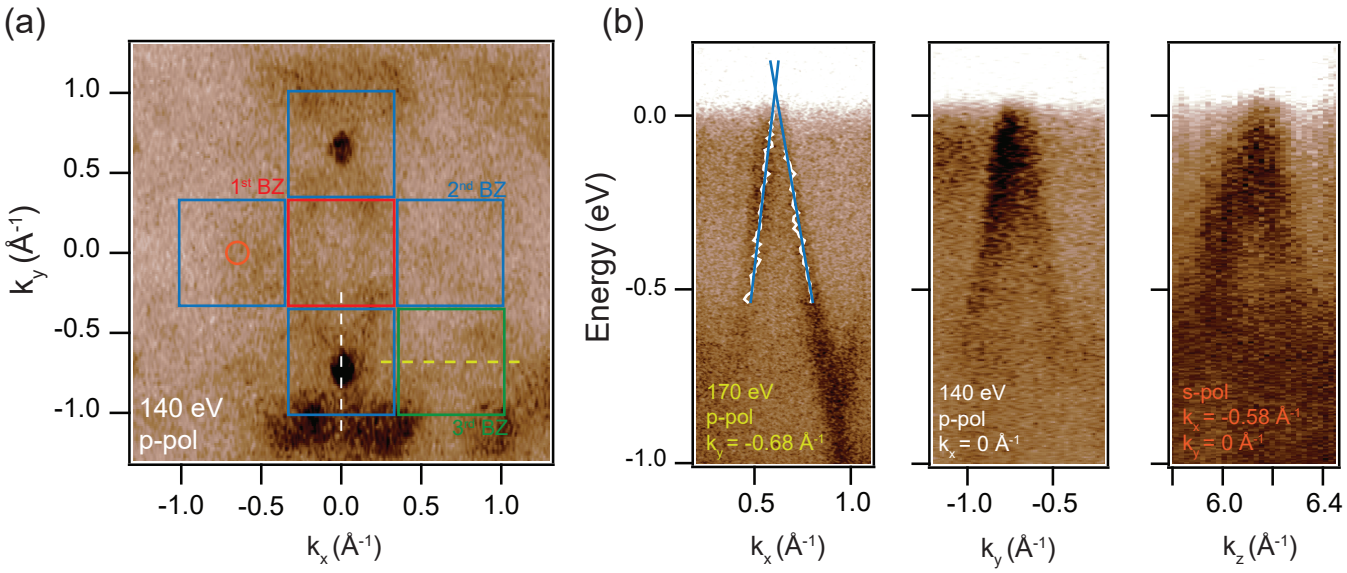

FIG. 2. $RhSb_3$ band structure as determined by photon-energy dependent ARPES at T=80 K. (a) Fermi surface at 140 eV, p-polarization. The red square shows the 1st surface-projected BZ for the (100) surface, while blue squares are the 2nd BZ and the green square the 3rd BZ. Intensity modulations away from Γ points are arguably due to surface state contributions (Suppl. Mat.) (b) ARPES band mapping along k_x, k_y and k_z directions. Left panel: band mapping along $k_y = -0.68\AA^{-1}$ line in the 3rd BZ, yellow dashed line in (a), 170 eV ($k_z \sim 5 \times 2\pi/c$), p-polarization. White solid curves show the peak position of the momentum distribution curves from a double-Gaussian fit, while blue solid lines are the result of a linear fit of the band dispersion. Central panel: band mapping along $k_x = 0\AA^{-1}$ line in the 2nd BZ, white dashed line in (a), 140 eV ($k_z \sim 4.5 \times 2\pi/c$), p-polarization. Right panel: kz dependence, assuming 10 eV inner potential, of the hole pocket in the 2nd BZ at $(k_x, k_y) = (-0.57\AA^{-1}, 0\AA^{-1})$; orange circle in (a), s-polarization.

(Fig. 3(c)). This temperature is sample dependent (See supplementary materials), but generally moves to higher temperature with increasing field. For instance, sample D exhibits semiconductor-like behavior up to 300 K in 14 T field.

Fig. 3(b) presents the Hall resistivity of $RhSb_3$ as a function of field at different temperatures. In fields below 6 T, the Hall resistivity $\rho_{xy}(T)$ is linear and barely shows any temperature-dependence, showing quantum oscillations at higher fields. Linear fitting of the low field Hall resistivity provides an estimate of the carrier density $n \sim 1.1 \times 10^{18}$ cm^{-3}, yielding a low-carrier-density system with only $\sim 10\%$ change with increasing temperature to room temperature, as shown in the inset of Fig. 3(c). This is consistent with the zero-gap band structure in Fig. 1(b). From the carrier density n and the zero-field resistivity $\rho_{xx} = 18\mu\Omega cm$, the classical mobility μ_c can be deduced from $1/\rho_{xx} = n\mu_c e$. The value of μ_c approaches 14 m^2/Vs at 1.8 K which decreases rapidly with increasing temperature. This value approaches that of graphene, Cd_3As_2 and TaAs/TaP (1-100 m^2/Vs).

Quantum oscillations measurements performed at varying temperatures and field orientations provide additional information on the effective carrier mass and FS, respectively. Quantum oscillations in conductivity are given by

$$\Delta\sigma_{xx}(T,B) = A(T,B)\cos\{2\pi[(F/B) - 1/2 + \beta]\}, \quad (1)$$

$$A(T,B) = e^{-2\pi^2 k_B T_D/\hbar\omega_c} \frac{2\pi^2 k_B T/\hbar\omega_c}{\sinh(2\pi^2 k_B T/\hbar\omega_c)} \quad (2)$$

where T_D is the Dingle temperature, $\omega_c = eB/m^*$ is the cyclotron frequency with m^* being the effective mass, β is the Berry phase and F is the SdH frequency of the oscillation corresponding to the the cross section of FS by the magnetic field [40]. One can clearly find that the oscillation of sample D in Fig. 3(a) and (b) has a very small frequency ($\sim$ 33 T). The SdH frequency F is given by the Onsanger relationship $F = \frac{\hbar\pi k_F^2}{2\pi e}$ with k_F being the Fermi wave vector, assuming four spheric Fermi pockets as an approximation. $F = 33(\pm 2)$ T gives $k_F = 0.04(5)\AA$ and a very small carrier density $n_{SdH} = 2.3(1) \times 10^{18}$ cm^{-3}, which is consistent with Hall resistivity results. Moreover, oscillations observed in Sample D appear to decay very slowly with increasing temperature, still being observable at 150 K.

The oscillations of sample E shows slightly higher frequency $F = 43$ T and the oscillations disappear at $\sim$ 100 K. Samples A and C exhibit larger oscillation frequencies (71 T for A and 60 T for C) which decay faster and disappear near 30 K and 50 K, respectively. This suggests the sample with smaller frequency and carrier

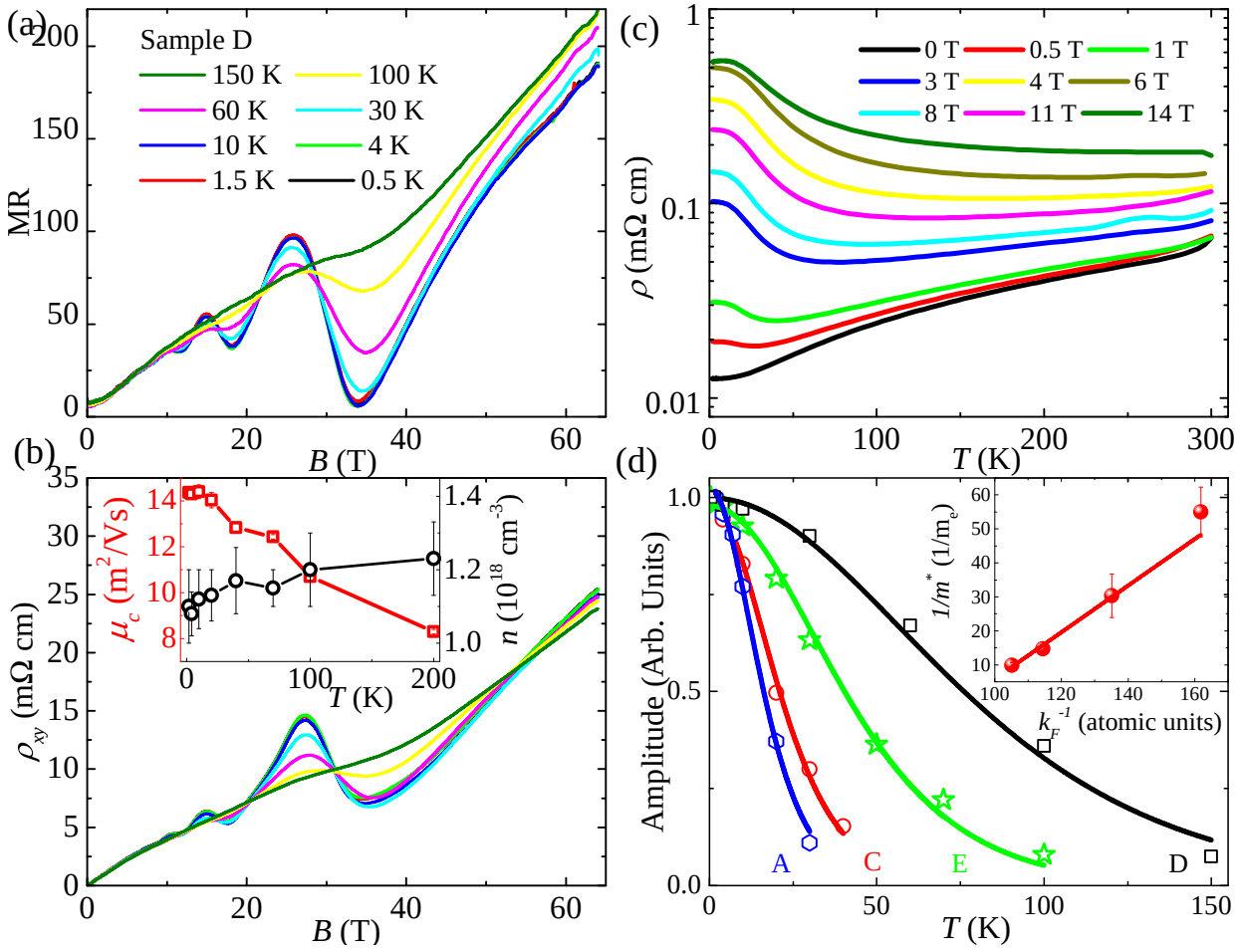

FIG. 3. Extremely large magnetoresistance, high carrier mobility and quantum oscillation of $RhSb_3$ single crystal. (a,b) Field dependence of the transverse resistivity (ρ_{xx}) and Hall resistivity (ρ_{xy}) at different temperatures with pulsed magnetic field up to 60 T. The inset in (b) shows the temperature dependence of the carrier mobility and density from the linear fitting of the low-field Hall resistivity. (c) Temperature dependence of the resistivity of sample D of $RhSb_3$ crystal with different magnetic fields. (d) The FFT amplitudes of the Fermi pocket as a function of temperature T, for sample A, C, D and E, respectively. The solid lines are the fits to Lifshitz-Kosevich formula. The effective mass for four samples increases with carrier density (oscillation frequency) increasing: Sample D F =33 T, $m^* = 0.015(7)m_e$; Sample E F = 43 T, $m^* = 0.033(4)m_e$; Sample C F = 60 T, $m^* = 0.086(7)m_e$; Sample E F = 71 T, $m^* = 0.102(8)m_e$. Inset: the linear fit (solid line) of $\frac{1}{m^*}$ versus $k_F^{-1} = \sqrt{\frac{\pi}{F}}$ for these four different samples (solid symbols).

density has carriers with smaller effective mass. The decaying of the amplitude of SdH oscillation with temperature is described by the Lifshitz-Kosevich (LK) formula $A(T, B)$ given by Eqn.(2). We track the FFT amplitude (Fig. 3(d)) for these samples, and fitting these data points to the LK formula gives the effective mass $m^* = 0.015(7)m_e, 0.033(4)m_e, 0.086(7)m_e$ and $0.102(8)m_e$ for sample E, D, C and A respectively. The effective mass in $RhSb_3$ is very light and is comparable to value of typical Dirac semimetal Cd_3As_2 ($0.023m_e$) and Weyl semimetals ($0.033m_e$ in NbAs, $0.076m_e$ in NbP and $0.15m_e$ in TaAs), consistent with Dirac-like carriers. The evolution of the effective mass with oscillation frequency/carrier concentration observed above also indicates the possible Dirac carriers. The effective mass, defined as $m^* = \hbar k_F/v_F$ should be constant for a parabolic band with different carrier densities since the Fermi velocity $v_F = \frac{1}{\hbar}\frac{\partial \varepsilon}{\partial k}|_{k_F} \propto k_F$ with ε being the band energy. But this is not true for Dirac fermions where v_F is a constant. In graphene, it is expected that the effective mass is proportional to the square root of carrier density since $k_F = (\pi n_s)^{1/2}$ and this was confirmed by several experiments [41, 42] Similar phenomenon has been observed in Cd_3As_2 [19]. The effective mass and Fermi vector in $RhSb_3$ follows above equation very well (inset of Fig. 3(d)) and gives the Fermi velocity $v_F \sim 1.3 \times 10^6$ m/s, which is consistent with the ARPES results and also close to that of Cd_3As_2 ($\sim 4 \times 10^6$ m/s) and Weyl semimetal NdP ($\sim 4.8 \times 10^5$ m/s). This large Fermi velocity and low effective mass is responsible for the high

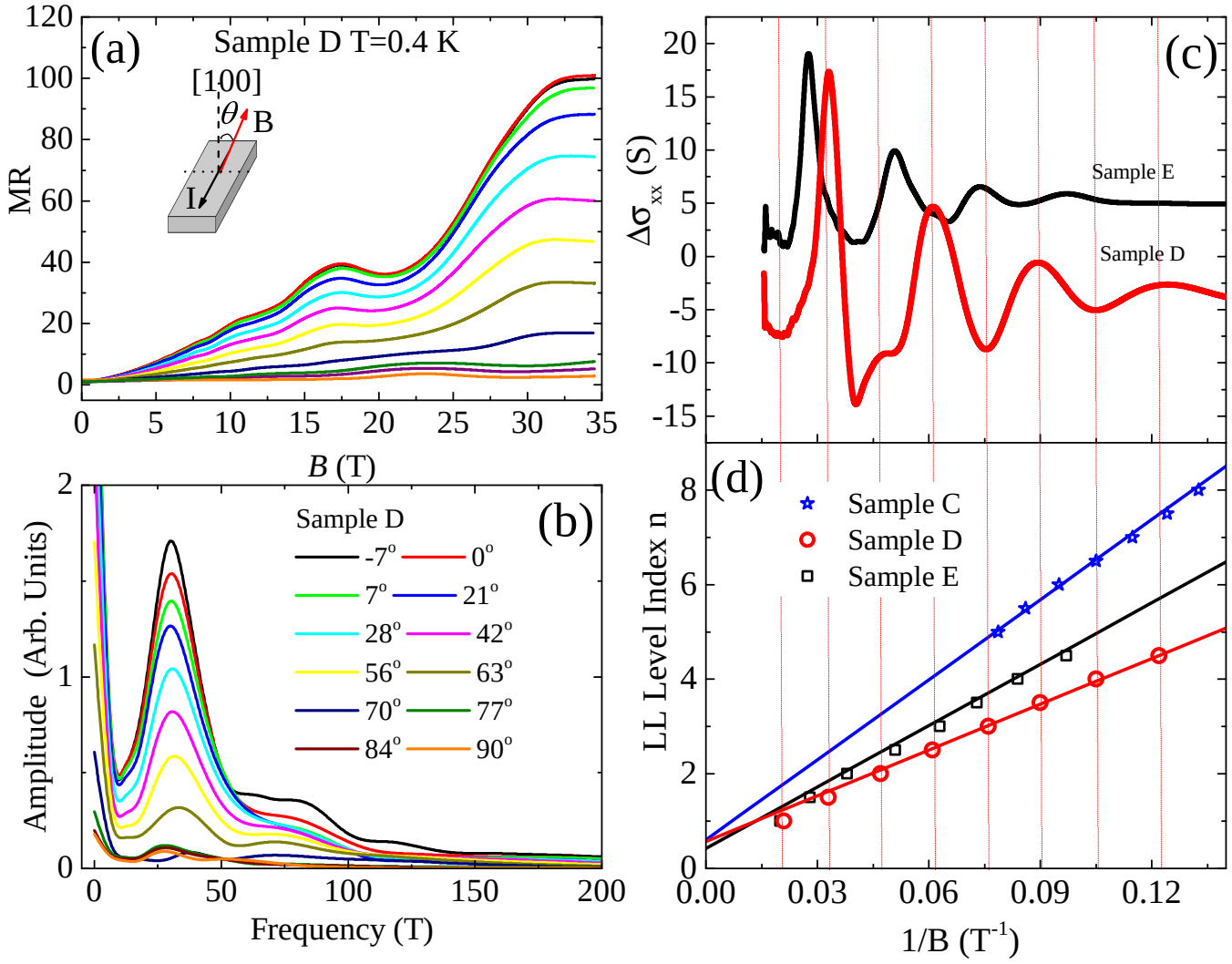

FIG. 4. (a) SdH oscillation at various magnetic field directions θ which was defined in the inset, in 0.4 K. (b) FFT spectrum of SdH oscillation in (a). The oscillation frequency ($F = 33$ T) rarely shows any angular dependence, indicating three-dimension Fermi pocket. (c) SdH oscillations $\Delta\sigma_{xx}$ as a function of $1/B$ in pulsed field up to 64 T for $RhSb_3$ cyrstal D and E. (d) Landau fan diagram. The black and green dotted lines mark the peak and dip positions respectively. The peaks of $\Delta\sigma_{xx}$ are assigned as integer Landau level indices and dips are assigned as half-integer indices. The linear extrapolation to the infinite field limit produces the intercepts of ~ 0.45, implying the Berry phase of π.

mobility observed in $RhSb_3$.

Surprisingly, the MR of $RhSb_3$, a cubic material, is highly anisotropic. The MR gradually disappears when the magnetic field is tilted from the [100] direction to the direction in the plane in sample D, as shown in Fig. 4(a). Fig. 4(b) also shows the FFT spectrum of the SdH oscillation with different field orientation for the origin data in Fig. 4(a). In sharp contrast to the MR, the oscillation frequencies (and therefore the FS cross-section) show very little dependence on field orientation, consistent with a three-dimension Fermi pocket. This is consistent with the electronic structure by both calculation and ARPES experiment, as discussed above. Fig. 4(c) shows the SdH oscillations $\Delta\sigma_{xx}$ as a function of $1/B$ for Sample D and E, both exhibiting clear periodicity. If we assign the maxima and minima of the SdH oscillations in $\Delta\sigma_{xx}$ as integer (n) and half-integer ($n + 1/2$), respectively, we can obtain the Landau fan diagram shown in Fig. 4(d). A linear extrapolation of n versus $1/B$ to the infinite field limit gives a finite intercept and therefore a finite Berry's phase, which should be zero for topologically trivial bands with parabolic dispersion, and π for a chiral Dirac dispersion. We find that the intercept for $RhSb_3$ is $\sim 0.4(6)$, giving $\beta = 0.9(2)\pi$ and therefore a nonzero Berry phase, implying a Dirac system with nontrivial topology.

Our experimental results suggest that $RhSb_3$ is a very low-density system where the carriers have extremely

light effective mass and very high mobility. Together with a nonzero Berry's phase and scaling of effective mass with Fermi velocity, this suggests that $RhSb_3$ is a three-dimensional Dirac semimetal, consistent with the linearly dispersing topological bulk bands revealed by calculation and ARPES. The large linear MR may be related to the presence of Dirac fermions, just as in other Dirac and Weyl materials [18–25], but there are several possible mechanisms that must also be considered. Quantum linear MR expected in the quantum limit, where all carriers are in the lowest Landau level [43], should not work here since the quantum limit field for $RhSb_3$ is larger than 35 T field, as shown by our quantum oscillation measurements. High mobility fluctuations due to the disorder effect is another possibility: if low mobility islands exist, the high mobility carriers will gain an effective drift velocity perpendicular to cycloid motion in an applied electric field because of the scattering, and the local current density will acquire a spatial fluctuation, giving a large linear MR.[19, 44, 45]. The change in FS induced by Zeeman splitting in field also was proposed for the extremely large MR in WTe_2 [46]. However, these mechanism cannot explain the highly anisotropic MR in $RhSb_3$ in parallel with a nearly isotropic 3D FS. One other possible explanation is the lifting of the protection mechanism for the highly conducting carriers.[18] The small residual resistivity ($\sim 15\ \mu\Omega$ cm) in $RhSb_3$ is indeed very small for such a low-carrier-density system, implying possible protection mechanisms for suppressing backscattering that would normally enhance resistivity. For $RhSb_3$, our first-principles calculations have revealed significant spin-orbit coupling. The time reversal invariant symmetry requires that the states at momenta k and $-k$ in bulk have opposite spin in the presence of spin-orbit coupling. This spin texture could also suppress backscattering. External fields will change the spin texture structure and lift the protection from back scattering, which ultimately induces the large MR. A similar mechanism has been discussed in the case of Cd_3As_2 [18], and the same bulk spin texture has also been proposed for WTe_2 with strong spin-orbit coupling and was believe to account for the circular dichroism in photoemission spectra [47]. In WTe_2 the magnetic field was found to have no influence on the FS but has a strong effect on the spin texture structure when field is along z direction, which well explains the anisotropic MR [47]. We believe that a similar mechanism is responsible for the anisotropic MR in $RhSb_3$, suggesting further study can verify this important mechanism for extreme magnetoresistance in topological semimetals.

SUMMARY

In summary, the electronic structure and transport properties of single crystals of the unfilled skutterudite material $RhSb_3$ were systematically studied by first-principle calculation and quantum oscillations measurements in magnetic fields up to 35 T. The electronic structure calculation indicates this material to be a zero-gap semimetal protected by symmetry with band inversion between Rh-4d and Sb-p orbitals. In the low-energy region below 20 meV, the bands are quasi-linear. $RhSb_3$ single crystals exhibit unsaturated MR up to $1.6 \times 10^4\%$ in 35 T field at 1.8 K. Quantum oscillations are consistent with the presence of very small three-dimensional hole pockets with a nontrivial Berry phase shift, suggesting a non-trivial topological aspect to this system. The extremely light effective mass of carriers increases from $0.015(7)m_e$ to $0.102(8)m_e$ as a function of the carrier density/Fermi vector in different crystals, consistent with a Dirac spectrum. Both the quantum oscillation and conventional Hall resistivity reveal a very large mobility ($\sim 14\ m^2$/Vs) which decreases with increasing temperature, while the carrier density shows very slight change. Our results postulate $RhSb_3$ as a member of a new family of three-dimensional Dirac semimetals whose electronic structure and topological properties deserve further attention.

This work was supported by the Gordon and Betty Moore Foundation?s EPiQS Initiative through Grant GBMF4419. Work at the National High Magnetic Field Laboratory is supported by the DOE NNSA DEFG52-10NA29659 (S. W. T and D. G.), by the NSF Cooperative Agreement No. DMR-0654118 and by the state of Florida.

[1] Hasan, M. Z. & Kane, C. L. Colloquium : Topological insulators. *Reviews of Modern Physics* **82**, 3045–3067 (2010). URL http://dx.doi.org/10.1103/RevModPhys.82.3045.

[2] Qi, X.-L. & Zhang, S.-C. Topological insulators and superconductors. *Reviews of Modern Physics* **83**, 1057–1110 (2011). URL http://dx.doi.org/10.1103/RevModPhys.83.1057.

[3] Young, S. M. *et al.* Dirac semimetal in three dimensions. *Phys. Rev. Lett.* **108** (2012). URL http://dx.doi.org/10.1103/PhysRevLett.108.140405.

[4] Wan, X., Turner, A. M., Vishwanath, A. & Savrasov, S. Y. Topological semimetal and fermi-arc surface states in the electronic structure of pyrochlore iridates. *Phys. Rev. B* **83** (2011). URL http://dx.doi.org/10.1103/PhysRevB.83.205101.

[5] Fang, C., Gilbert, M. J., Dai, X. & Bernevig, B. A. Multi-weyl topological semimetals stabilized by point group symmetry. *Phys. Rev. Lett.* **108** (2012). URL http://dx.doi.org/10.1103/PhysRevLett.108.266802.

[6] Bzdušek, T., Wu, Q., Regg, A., Sigrist, M. & Soluyanov, A. A. Nodal-chain metals. *Nature* **538**, 75–78 (2016). URL http://dx.doi.org/10.1038/nature19099.

[7] Burkov, A. A., Hook, M. D. & Balents, L. Topological nodal semimetals. *Phys. Rev. B* **84** (2011). URL http://dx.doi.org/10.1103/PhysRevB.84.235126.

[8] Wang, Z. *et al.* Dirac semimetal and topological phase transitions in a 3 Bi (a = na , k, rb). *Phys. Rev. B* **85** (2012). URL http://dx.doi.org/10.1103/PhysRevB.85.195320.

[9] Wang, Z., Weng, H., Wu, Q., Dai, X. & Fang, Z. Three-dimensional dirac semimetal and quantum transport in cd 3 As 2. *Phys. Rev. B* **88** (2013). URL http://dx.doi.org/10.1103/PhysRevB.88.125427.

[10] Borisenko, S. *et al.* Experimental realization of a three-dimensional dirac semimetal. *Phys. Rev. Lett.* **113** (2014). URL http://dx.doi.org/10.1103/PhysRevLett.113.027603.

[11] Neupane, M. *et al.* Observation of a three-dimensional topological dirac semimetal phase in high-mobility cd3As2. *Nature Communications* **5** (2014). URL http://dx.doi.org/10.1038/ncomms4786.

[12] Liu, Z. K. *et al.* A stable three-dimensional topological dirac semimetal cd3As2. *Nature Materials* **13**, 677–681 (2014). URL http://dx.doi.org/10.1038/nmat3990.

[13] Jeon, S. *et al.* Landau quantization and quasiparticle interference in the three-dimensional dirac semimetal cd3As2. *Nature Materials* **13**, 851–856 (2014). URL http://dx.doi.org/10.1038/nmat4023.

[14] Lv, B. Q. *et al.* Experimental discovery of weyl semimetal TaAs. *Phys. Rev. X* **5** (2015). URL http://dx.doi.org/10.1103/PhysRevX.5.031013.

[15] Xu, S.-Y. *et al.* Discovery of a weyl fermion semimetal and topological fermi arcs. *Science* **349**, 613–617 (2015). URL http://dx.doi.org/10.1126/science.aaa9297.

[16] Soluyanov, A. A. *et al.* Type-II weyl semimetals. *Nature* **527**, 495–498 (2015). URL http://dx.doi.org/10.1038/nature15768.

[17] Huang, L. *et al.* Spectroscopic evidence for a type II weyl semimetallic state in MoTe2. *Nature Materials* **15**, 1155–1160 (2016). URL http://dx.doi.org/10.1038/nmat4685.

[18] Liang, T. *et al.* Ultrahigh mobility and giant magnetoresistance in the dirac semimetal cd3As2. *Nature Materials* **14**, 280–284 (2014). URL http://dx.doi.org/10.1038/nmat4143.

[19] Narayanan, A. *et al.* Linear magnetoresistance caused by mobility fluctuations in n -doped cd 3 As 2. *Phys. Rev. Lett.* **114** (2015). URL http://dx.doi.org/10.1103/PhysRevLett.114.117201.

[20] Wang, Z. & Zhang, S.-C. Chiral anomaly, charge density waves, and axion strings from weyl semimetals. *Phys. Rev. B* **87** (2013). URL http://dx.doi.org/10.1103/PhysRevB.87.161107.

[21] Shekhar, C. *et al.* Extremely large magnetoresistance and ultrahigh mobility in the topological weyl semimetal candidate NbP. *Nat Phys* **11**, 645–649 (2015). URL http://dx.doi.org/10.1038/nphys3372.

[22] Li, Q. *et al.* Chiral magnetic effect in ZrTe5. *Nature Physics* **12**, 550–554 (2016). URL http://dx.doi.org/10.1038/nphys3648.

[23] Chenglong Zhang, S. X. Z. L. B. T. M. Z. H. J. W. C. Z. S. J., Zhujun Yuan. Tantalum monoarsenide: an exotic compensated semimetal. URL https://arxiv.org/abs/1502.00251.

[24] Huang, X. *et al.* Observation of the chiral-anomaly-induced negative magnetoresistance in 3d weyl semimetal TaAs. *Phys. Rev. X* **5** (2015). URL http://dx.doi.org/10.1103/PhysRevX.5.031023.

[25] Luo, Y. *et al.* Electron-hole compensation effect between topologically trivial electrons and nontrivial holes in NbAs. *Phys. Rev. B* **92** (2015). URL http://dx.doi.org/10.1103/PhysRevB.92.205134.

[26] Ali, M. N. *et al.* Large, non-saturating magnetoresistance in WTe2. *Nature* (2014). URL http://dx.doi.org/10.1038/nature13763.

[27] Tafti, F. F., Gibson, Q. D., Kushwaha, S. K., Haldolaarachchige, N. & Cava, R. J. Resistivity plateau and extreme magnetoresistance in LaSb. *Nature Physics* **12**, 272–277 (2015). URL http://dx.doi.org/10.1038/nphys3581.

[28] Wang, K., Graf, D., Li, L., Wang, L. & Petrovic, C. Anisotropic giant magnetoresistance in NbSb2. *Sci. Rep.* **4**, 7328 (2014). URL http://dx.doi.org/10.1038/srep07328.

[29] Shen, B., Deng, X., Kotliar, G. & Ni, N. Fermi surface topology and negative longitudinal magnetoresistance observed in the semimetal NbAs 2. *Physical Review B* **93** (2016). URL http://dx.doi.org/10.1103/PhysRevB.93.195119.

[30] Luo, Y. *et al.* Anomalous electronic structure and magnetoresistance in TaAs2. *Scientific Reports* **6**, 27294 (2016). URL http://dx.doi.org/10.1038/srep27294.

[31] Tang, Y. *et al.* Convergence of multi-valley bands as the electronic origin of high thermoelectric performance in CoSb3 skutterudites. *Nature Materials* **14**, 1223–1228 (2015). URL http://dx.doi.org/10.1038/nmat4430.

[32] Singh, D. J. & Pickett, W. E. Skutterudite antimonides: Quasilinear bands and unusual transport. *Phys. Rev. B* **50**, 11235–11238 (1994). URL http://dx.doi.org/10.1103/PhysRevB.50.11235.

[33] Smith, J. C., Banerjee, S., Pardo, V. & Pickett, W. E. Dirac point degenerate with massive bands at a topological quantum critical point. *Phys. Rev. Lett.* **106** (2011). URL http://dx.doi.org/10.1103/PhysRevLett.106.056401.

[34] Pardo, V., Smith, J. C. & Pickett, W. E. Linear bands, zero-momentum weyl semimetal, and topological transition in skutterudite-structure pnictides. *Phys. Rev. B* **85** (2012). URL http://dx.doi.org/10.1103/PhysRevB.85.214531.

[35] Yang, M. & Liu, W.-M. The d-p band-inversion topological insulator in bismuth-based skutterudites. *Sci. Rep.* **4** (2014). URL http://dx.doi.org/10.1038/srep05131.

[36] Weinert, M., Wimmer, E. & Freeman, A. J. Total-energy all-electron density functional method for bulk solids and surfaces. *Phys. Rev. B* **26**, 4571–4578 (1982). URL http://dx.doi.org/10.1103/PhysRevB.26.4571.

[37] P. Blaha, G. K. H. M. D. K. J. L., K. Schwarz. *An Augmented PlaneWave + Local Orbitals Program for Calculating Crystal Properties* (Karlheinz Schwarz, Techn. Universitat Wien, Austria, 2001). URL http://www.wien2k.at/.

[38] Perdew, J. P., Burke, K. & Ernzerhof, M. Generalized gradient approximation made simple. *Phys. Rev. Lett.* **77**, 3865–3868 (1996). URL http://dx.doi.org/10.1103/PhysRevLett.77.3865.

[39] Fu, L. & Kane, C. L. Topological insulators with inversion symmetry. *Physical Review B* **76** (2007). URL http://dx.doi.org/10.1103/PhysRevB.76.045302.

[40] Shoenberg, D. *Magnetic oscillations in metals* (Cambridge University Press (CUP), 1984). URL http://dx.doi.org/10.1017/CBO9780511897870.

[41] Neto, A. H. C., Guinea, F., Peres, N. M. R., Novoselov, K. S. & Geim, A. K. The electronic properties of graphene. *Reviews of Modern Physics* **81**, 109–162 (2009). URL http://dx.doi.org/10.1103/RevModPhys.81.109.

[42] Novoselov, K. S. *et al.* Two-dimensional gas of massless dirac fermions in graphene. *Nature* **438**, 197–200 (2005). URL http://dx.doi.org/10.1038/nature04233.

[43] Abrikosov, A. A. Quantum linear magnetoresistance. *Europhysics Letters (EPL)* **49**, 789–793 (2000). URL http://iopscience.iop.org/0295-5075/49/6/789).

[44] Kozlova, N. *et al.* Linear magnetoresistance due to multiple-electron scattering by low-mobility islands in an inhomogeneous conductor. *Nature Communications* **3**, 1097 (2012). URL http://dx.doi.org/10.1038/ncomms2106.

[45] Hu, J. & Rosenbaum, T. F. Classical and quantum routes to linear magnetoresistance. *Nature Materials* **7**, 697–700 (2008). URL http://dx.doi.org/10.1038/nmat2259.

[46] Rhodes, D. *et al.* Role of spin-orbit coupling and evolution of the electronic structure of WTe 2 under an external magnetic field. *Physical Review B* **92** (2015). URL http://dx.doi.org/10.1103/PhysRevB.92.125152.

[47] Jiang, J. *et al.* Signature of strong spin-orbital coupling in the large nonsaturating magnetoresistance material WTe 2. *Physical Review Letters* **115** (2015). URL http://dx.doi.org/10.1103/PhysRevLett.115.166601.